ACS OMEGA

http://pubs.acs.org/journal/acsodf

Article

Customizing the Appearance of Sparks with Binary Metal Alloys

Philipp Memmel, Felix Lederle, Martin Söftje, Jannis Koch, Mingji Li, Wolfgang Schade, and Eike G. Hübner*

Cite This: https://doi.org/10.1021/acsomega.2c03081

Read Online

ACCESS | Metrics & More | Article Recommendations | Supporting Information

ABSTRACT: Long-flying sparks are an essential part of several pyrotechnic effects. Unfortunately, and in contrast to colored flames, the color space of sparks is basically limited to the black body curve. With low-boiling-point metals, vapor-phase combustion and bright colorful flashes are achievable. Since 1999, alloys of rare-earth elements have been proposed for colorful spark generation. To the best of our knowledge, here, we present the first investigation of such alloys to change the color of sparks beyond the black body limit. Alloys consisting of >65 at. % of a brightly emitting and low-boiling-point metal and a carrier metal allow achieving long-flying deeply colored sparks. Besides the color, branching of sparks is crucial for the visual appearance. Rare-earth metals were found to promote branching of different alloys. Finally, fountains ejecting golden/green sparks based on a stable eutectic Yb−Cu alloy and continuously branching sparks based on $Nd_2Fe_{14}B$ are presented.

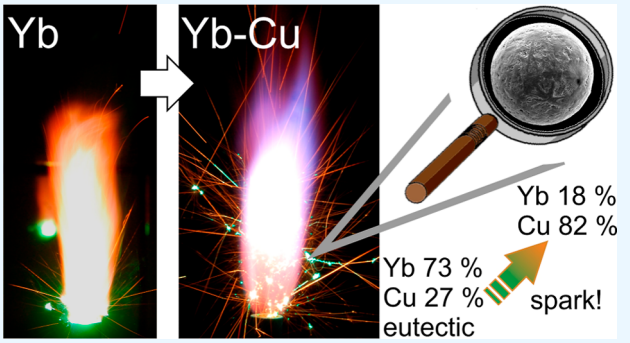

INTRODUCTION

Sparks are typically formed by incandescent metal particles and are part of numerous pyrotechnic compositions and firework effects. Various materials have been investigated for spark generation.[1−4] Besides pure elements such as iron, aluminum, and titanium, alloys such as MgAl (magnalium), Al_2Zr (zircalium), Mg−Zn, Zr−Ni, Fe−Ti (ferrotitanium), Fe−Al (ferroaluminum), TiC, and Fe−Zr (ferrozirconium) are used.[1,5−11] In any case, the color of the spark is controlled by black/gray body radiation, that is, the temperature of the particle heated by surface combustion. Accordingly, the color space is limited to the black body curve and ranges from dark red to typically yellow/golden and bright white.[1] In contrast, the color of a flame can be controlled by element-specific emission processes in the gaseous phase to match most visible colors.[12] Rare-earth elements have been proposed to burn in the gaseous state and to form temperature-stable monoxides as colorful emitters in the flame.[13] Beginning in 2011, Koch investigated polytetrafluoroethylene (PTFE)-containing pyrotechnic formulations based on Yb, Sm, Eu, and Tm as fuel, which form bright colorful flashes and short, thick sparks.[14−17] Unfortunately, vapor-phase combustion is accompanied by fast consumption of the metal, and the resulting sparks appear more as flashes.[18]

To predict surface or vapor-phase combustion, Glassman's criterion based on the boiling point of the metal and the reaction product (metal oxide) is discussed critically in the literature. It is not straightforward to apply due to uncertainties of the boiling points of metal oxides. Often, dissociation processes instead of true boiling take place.[19] While computer simulations are necessary to provide a reliable prediction,[19] Gordon's limit as a very rough rule of thumb provides a helpful classification for deciding if vapor-phase combustion is likely to dominate the spark's appearance.[20] Gordon's limit for substances in Class A (gas-phase combustion) is given around 1500 °C for the boiling point of the element. Indeed, rare-earth elements such as Yb, Eu, or Sm boiling below or around this temperature form colorful flashes, as described above.[14,18] In contrast, high-boiling-point rare-earth elements such as Lu (bp. 3400 °C) form sparks that are dominated by black body radiation.[18] In view of long flying colorful sparks, the most interesting elements are rare-earth metals with a boiling point above Gordon's limit to prevent immediate vaporization but not so high as to exclude vapor-phase combustion. Sparks based on Er (bp. 2870 °C) reach a significant length and show a distinct color change from golden-white black body radiation to bright green vapor-phase combustion (Figure 1a).[18,21] The radiation jump in brightness, accompanied by colorful gas-phase combustion, is congruent with the burning behavior of other metals and can partially be explained by metal−oxygen phases with a significantly reduced boiling point.[22] Unfortunately, as visualized in Figure 1a, the colorful phase is rather short and the overall sparks brightness is so high that the green color does not dominate the spark's appearance. The near-infrared (NIR) image (Figure 1a, right) reveals the unchanged underlying black body emission of the incandescent erbium

Received: May 17, 2022
Accepted: July 14, 2022

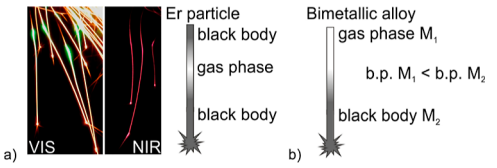

Figure 1. a) Color-changing sparks based on erbium powder[18,21] and (b) sketch of the concept investigated here for color-changing sparks based on binary metal alloys.

particle during the colorful phase, in sum leading to a green-white appearance. From the view of deeply colored sparks, a longer colored phase as well as a significantly lower spark temperature to minimize the underlying black body emission would be desirable.

In 1999, Sturman suggested rare-earth metal-containing alloys for colored spark formation.[13] Here, we investigated 11 commercial and targetedly synthesized alloys and six rare-earth elements to elucidate the concept of color-changing sparks based on a low-boiling-point fast-burning and colorful emitting element, which is diluted with a high-boiling-point or less reactive element (Figure 1b). We report on deep green spark segments based on eutectic Yb−Zn and Yb−Cu powders as well as deep red spark segments based on "Li_3Si" powder (as a mixture of Zintl phases).

Besides the color, branching is a crucial aspect of the spark's appearance.[1] Branching of iron sparks is well-known from commercial "sparklers", which emit incandescent iron. Each spark is terminated after a few centimeters by an intense branching event. In the case of iron, branching is promoted by a carbon content of around 0.7 wt. %. One explanation given in the literature is based on the resulting heterogeneous microstructure of α-Fe and cementite, which leads to Fe_3C-rich and Fe_3C-free domains. Upon oxidation, Fe_3C releases CO_2, which leads to internal pressure and initiates bursting of the spark.[23] Various other metals that are free of carbon show extensive branching. Examples include titanium, magnalium, Mg−Zn, mischmetal, and other alloys.[10,11] In general, trapped gases and a resulting internal pressure are given as the explanation.[22,24] Internal voids, which can be seen as a preliminary step to branching, are detected in quenched spark droplets of various materials.[22] These voids are formed by the gas release from the metal−gas solution of the burning particle. A temperature increase of the particle subsequently leads to expansion of the gas and particle explosion.[22] In the case of alloys, the internal pressure can be caused by intraparticle boiling of the lower-boiling-point element, which again leads to microexplosions of the particle.[10] Here, we observed a fraction of rare-earth metals in alloys promoting branching and report on a pyrotechnic composition based on $Nd_2Fe_{14}B$, which emits sparks with several stages of branching.

RESULTS AND DISCUSSION

To analyze the influence of diluting rare-earth metals with higher-boiling-point and/or less reactive metals on spark formation, various rare-earth metal-containing alloys have been investigated. Elements and alloys have been rasped to a coarse powder using a diamond-coated rasp in a glovebox if not obtained as a powder. Particle sizes have been measured by laser scanning microscopy and are averaged across 50−100 particles. Alloys have been prepared from the elements if necessary (see below). Powders have been passed into the invisible flame of a methane/air burner and monitored by long-time exposures, NIR photography, and time-resolved fiber optical emission spectroscopy with a short integration time of 1 ms to distinguish between phases of surface and vapor-phase combustion. Spark temperatures have been obtained from Planck fits of the emission spectra of surface combustion phases with a correlation of determination of $R^2 \geq 0.99$ (Yb−Cu, Yb−Zn: 0.98) in all cases. Alloys and recovered burned

Table 1. Physical and Optical Properties of the Elemental Metals Discussed Here and the Sparks Formed Therefrom

metal	bp.[28,29] (°C)	ΔH_c[a] (kJ mol^{-1})	bp. stable oxide (°C)	electronegativity[29]	Dom. WL[b] (nm)	Dom. emitter[c]	Sp. purity[b] (%)	temperature[d] (K)
Fe	2861	−412.1	(dec. FeO: 3405)[e,19,30]	1.83	589	bb	82	2054 ± 4.0
Co	2927	−297.0		1.88				
Ni	2913	−244.8		1.91				
Si	3265	−910.7	2950[29]	1.90				
Al	2470	−837.9	2977[31]	1.61				
Cu	2562	−157.3	(dec. Cu_2O: 1800)[29]	1.90				
Zn	907	−350.5	(dec. ZnO: 1974)[29]	1.65				[f]
Li	1342	−299.0	2468[32] (subl. >1000)[33]	0.98				
Ca	1487	−634.9	2850[34]	1.00				
Er	2868	−949.0	3920[e,35]	1.24	584 (s)	bb	63	2680[18]
					562 (g)	ErO	28	
					584 (s)	bb	63	
Y	2930	−952.7	4300[e,36]	1.22	583 (s)	bb	60	2930[18]
					587 (g)	YO	53	
Sm	1794	−911.5	3780[e,35]	1.17	607 18	SmO, Sm	38[18]	[f]
Yb	1193	−907.3	4070[e,35]	1.10	565	YbO(H)	26	[f]
Ce	3443	−898.1	3730[e,35]	1.12	585	bb	63	2770 ± 3
La	3464	−896.9	3620[e,35]	1.10	586	bb	64	2669 ± 4
Nd	3074	−904.0	3760[e,35]	1.14	584	bb (NdO)	64	2718 ± 2

[a]Calcd. from the heat of formation of the stable oxide.[29] [b]Dominant wavelength (WL) and spectral (Sp.) purity determined by emission spectroscopy and the CIE 1931 diagram. [c]Species dominating the emitted wavelength,[27] bb = black body emission. [d]Spark temperature determined by the Planck fit of the emission spectra. [e]Boiling or dissociation temperature. [f]Only vapor-phase combustion.

https://doi.org/10.1021/acsomega.2c03081
ACS Omega XXXX, XXX, XXX−XXX

Table 2. Physical and Optical Properties of the Alloys Discussed Here and the Sparks Formed Therefrom

alloy	composition[a] (at. %)	ΔH_c[b] (kJ mol·atoms^{-1})	composition after burning	Dom. WL[g] (nm)	Dom. emitter[h]	Sp. purity[g] (%)	temperature[j] (K)
"Li_3Si"	Li: 76[d]; Si: 24	−426.4[48]	(99 at. % Si)[k]	C-494[l](g)	Li, SiO2	78	1971 ± 5
				671 (peak)	Li	100	
				589 (s)	bb	86	
$CaSi_2$	Ca: 36; Si: 64	−781.0[49]	unchanged[e]	588	bb (CaO)	79	2121 ± 8
			30−50 at. % Ca				
Yb_3Si_5	Yb: 37[d]; Si: 63	−868.1[41]	60−90 at. % Si[e]	592	bb	89	1711 ± 4
			av.: 77 at. % Si				
$SmCo_5$	Sm: 16; Co: 84	−378.1	unchanged[e]	588	bb	79	2130 ± 6
			10−15 at. % Sm				
$Nd_2Fe_{14}B$	Nd: 12; Fe: 82[c]	−475.3	unchanged	588	bb	79	2142 ± 6
			9−13 at. % Nd				
$LaNi_5$	La: 17; Ni: 83	−332.0	approx. 50 at. % La[e]	588	bb	81	2100 ± 7
ferrocerium	RE: 69[i,e]; Fe: 21; Mg: 10	∼800	RE: 70−80; Fe: 20−30[e]	584	bb	62	2815 ± 4
			Mg: 0 at. %				
Y_3Co	Y: 76; Co: 24	−772.8	approx. 98-at. % Y	586	bb	68	2479 ± 3
Y_2Al	Y: 67; Al: 33	−864.2	approx. 98 at. % Y	585	bb (YO)	63	2759 ± 2
Yb−Cu	Yb: 73; Cu: 27	−694.9	60−99 at. % Cu	569 (g)	YbO(H)	35	1551 ± 11
			av.: 82 at. % Cu	594 (s)	bb	91	
Yb−Zn	Yb: 73; Zn: 27	−736.4	[f]	550 (g)	YbO(H)	27	1645 ± 10
				592 (s)	bb	91	

[a]Given by the supplier and measured by EDX. [b]Estimated from the heat of formation values of the oxides[29] and the alloy. ΔH_f of alloys estimated by the Miedema model[26] if not noted differently. [c]Contains 1 wt. % of boron. [d]From inductively coupled plasma optical emission spectroscopy. [e]Broad range/phase separation. [f]No burned particles recovered. [g]Dominant wavelength (WL) and spectral (Sp.) purity determined by emission spectroscopy and the CIE 1931 diagram. [h]Atomic/molecular species dominating the emitted wavelength,[27] bb = nonspecific black body emission. [i]Sum of Ce, La, and other rare-earth (RE) elements. [j]Spark temperature determined by the Planck fit of the emission spectrum. [k]Li not detected by EDX. [l]Complementary wavelength in the CIE 1931 diagram.

particles have been analyzed by scanning electron microscopy (SEM) and energy-dispersive X-ray spectroscopy (EDX) to gather information about the change of the metal ratio (see Figure S20 of the Supporting Information). Although the composition analysis results in a rather broad range and is partially affected by phase separation of the metal oxides, the comparison of several particles per alloy and across several alloys reveals some consistent trends. Properties of relevant elements including heat of combustion and electronegativity to discuss reactivity as well as dominant wavelength/spectral purity (calculated from the chromaticity diagram) of the spark and spark temperatures are given in Table 1. The heat of combustion of alloys has been calculated according to their composition, and the heat of formation of the alloys has been taken into account with help of the Entall Miedema calculator.[25,26] The elemental ratio before and after the burning of alloys as well as the corresponding spark's wavelength/spectral purity and temperature is given in Table 2. Spark lengths are evaluated from scaled photographic images and are averaged across 15−25 spark events. Details concerning particle size distribution and spark length are given in Table 3.

The basic effect of alloying a rare-earth element on spark formation is visualized by yttrium. Pure Y shows a long spark based on surface combustion with a bright, short red phase of vapor-phase combustion (Figure 2a). The red phase is reflected by two broad peaks around 605 and 625 nm in the emission spectra, caused by a matching series of emission bands from the high-temperature stable emitter YO (Figure 3c).[18,27] Moving from Y to the stable intermetallic compound Y_2Al significantly weakens the bright red phase (Figure 2b). It is less pronounced, and the spark's color seems to be only slightly shifted to the red. This is backed by the emission spectrum of the spark revealing only a slight increase on the black body curve (Figure 3c). The position of the weak peak still matches with the expected YO bands. The temperature of the Y_2Al spark is reduced from 2930 K (Y) to 2760 K (Y_2Al), which is in agreement with the minimized evaporation and the resulting reduced vapor-phase combustion of high-boiling-point Y (bp. 3203 K). The reasons for the reduced spark temperature are the reduced reactivity of Al compared to that of Y (electronegativity is increased by 0.39 from Y to Al and ΔH_c is reduced by 88.5 kJ mol·atoms^{-1} for Y_2Al compared to that for Y) and the lower boiling point of Al. In fact, the spark's temperature of 2760 K matches quite exactly the boiling point of Al (2743 K). The assumption of a loss of Al by evaporation is confirmed by the EDX measurements of the burned particles. While the expected composition of Y_2Al powder is reflected by EDX, the burned particles recovered after spark formation reveal a metal fraction of approx. 98 at. % Y. Consequently, it may be concluded that Al evaporated during the burning process. Interestingly, the burned particles revealed a hollow, egg-shell-like appearance (Figure 4a). The formation of voids up to hollow particles in quenched sparks has been investigated in detail by Dreizin.[22] Voids as well as hollow oxides are observed during oxidation processes of various metal powders.[22,37,38]

Replacing aluminum with cobalt by means of the stable compound Y_3Co confirms these observations. Despite the higher Y content, the heat of combustion is reduced further by an additional 91.4 kJ mol·atoms^{-1}, and the oxophilicity of cobalt is reduced in comparison to that of aluminum. Consequently, the emission spectrum (Figure 3c) and the long-time exposure (Figure S28 of the Supporting Information) did not reveal any red colored phases of vapor-phase combustion, and the spark's temperature is reduced to 2479 K.

https://doi.org/10.1021/acsomega.2c03081
ACS Omega XXXX, XXX, XXX−XXX

Table 3. Particle Sizes of Elemental Metal Powders and Alloys Discussed Here as Well as Characteristics of Sparks

metal powder	D^a (μm)	spark length (cm)	rel. thickness
Fe	77−156	11−16	1−2
Ce	115−249	5−9	4
La	95−222	4−10	2
ferrocerium	58−225	-[b]	
Nd	67−269	5−15[b]	3
$Nd_2Fe_{14}B$	18−123	8−13	2
$LaNi_5$	3−7	12−21	1
$SmCo_5$	13−80	13−24	1−2
Y	75−220	4.5−9[b,c]	
	stage 1 (s):	1−1.5	2
	stage 2 (g):	0.5[c]	3−5
	stage 3 (s):	3−7[b]	3
Y_2Al	20−176	3−6[b]	
	stage 1 (s):	1−1.5	2
	stage 2 (sg):	2−4.5[b]	3
Y_3Co	34−101	3−7[b]	2
Yb	55−312		
Yb_3Si_5	4−31	5−8	1
Yb−Cu	10−84	3−6[d]	
	stage 1 (g):	1−2[d]	4−5
	stage 2 (s):	2−4[d]	2−3
Yb−Zn	66−202	1.3−3[d]	
	stage 1 (g):	0.3−1.5[d]	1−3
	stage 2(s):	1−1.5[d]	1
$CaSi_2$	31−86	5−8	1−2
"Li_3Si"	51−224	6−20	
	stage 1 (g):	3−4	3
	stage 2 (s):	3−16	3

[a]Approx. grain size measured by confocal laser microscopy. [b]Limited by branching. [c]Gas-phase combustion fades into surface combustion. [d]Repeated multiple stages of vapor-phase and surface combustion.

Obviously, the high boiling point of Y prevents the formation of long colored spark phases. $SmCo_5$, which is a common material for rare-earth magnets, was investigated next. Pure Sm with a significantly lower boiling point of 1794 °C forms bright red flashes (the inset of Figure 2c).[18] In contrast, $SmCo_5$ forms long golden sparks, which are reminiscient of iron sparks. The photographic image (Figure 2c) reveals the absence of red vapor-phase combustion or even a red corona, which is confirmed in the emission spectrum (Figure S3 of the Supporting Information). No indication for emission from SmO around 650 nm could be recognized.[27] The spark temperature of 2130 K is just above the boiling point of Sm, but apparently, the low concentration of 16 at. % Sm in $SmCo_5$ prohibits the formation of element-specific emitting vapor-phase combustion.

Based on these results, Yb alloys were investigated. Yb provides a lower boiling point (1193 °C) and intense green emission, which significantly differs from black body emitters. As visualized in Figure 2d, pure Yb forms bright explosive flashes, which do not extend to longer flying sparks.[18] The Zintl-phase Yb_3Si_5 provides a rather promising composition with 37 at. % Yb. Unfortunately, after contact with a flame, only dark golden-red sparks are observed (Figure 2e). The emission spectrum (Figure 3a) is well-fitted by the black body curve and represents a spark temperature of 1711 K, which would be high enough to evaporate Yb. The broad emission bands of YbO around 480 and 544 nm as well as the emission band from YbOH at 533 nm[18,27] are absent, and solely the additional emission of sodium (589 nm) and lithium (671 nm) in the gas flame was observed. Lithium is a reductant for the preparation of rare-earth elements, and residues of Li and Na are found in Yb.[39,40] Possible reasons for the absence of vapor-phase combustion are the reduced reactivity of Si, albeit having comparable heats of combustion (reduced by 39.2 kJ mol·atoms^{-1} for Yb_3Si_5 vs Yb due to its heat of formation), and the partly ionic nature of the Zintl phase. The electronegativities of Yb and Si differ by 0.8, and an average valence state of 2.5 is assumed for Yb_3Si_5 with di- and trivalent Yb.[41,42] Finally, the fraction of 37 at. % Yb might still be too low. Based on the previously described experiments, a rare-earth content of ∼70 at. % would be desirable. Looking through the binary phase diagrams of Yb, only a few stable intermetallic compounds with a high Yb content such as Ag_3Yb_5, Au_3Yb_7, or $GaYb_2$ were identified and not classified as useful.[43] Therefore, we decided to prepare the eutectic alloys Yb−Cu and Yb−Zn with 73 at. % Yb.[43] Cu and Zn can be considered as nontoxic and stable, and they are commonly used in pyrotechnic compositions. The eutectics provide rather low melting points for a convenient synthesis, and as eutectic mixtures, the solidified melt should appear homogeneous on the scale of metal powders discussed here (100 μm). Both eutectics have been prepared following a procedure given in the literature by melting the elements in sealed quartz tubes at 900/1100 °C under vacuum.[44] In both cases, the resulting alloys have been proven by SEM/EDX to consist of equimolar YbZn or YbCu phases, respectively, with ytterbium-rich fractions containing 90 at. % Yb (Yb−Zn) or 88 at. % Yb (Yb−Cu), as expected according to the phase diagram.[43] Yb−Zn and Yb−Cu alloys have been analyzed in detail in the literature.[45,46] The eutectics show phase separation on a scale of approx. 10 μm.[45]

Both alloys appeared as silvery, brittle, and stable material (see below). Upon contact with a flame, Yb−Cu bursts into a shower of golden and green sparks (Figure 2g). In contrast to pure Yb, the sparks are transported outside of the flame and reveal a considerable length of 3−6 cm. The sparks appear as a mixture of golden surface combustion, green flashes of vapor combustion, and color-changing sparks with deep green (1−2 cm) and golden (2−4 cm) stages. Interestingly, the spark phases can be repeated several times. The change from green to golden occurs as a slow fading out, while the change from golden to green appears suddenly, often combined with a branching event. In Figure 2g, which shows a single ignited portion of metal powder, only some isolated green sparks are visible. Fortunately, if emitted from a longer burning pyrotechnic composition, long colored sparks are continuously generated (see below). The emission spectra of the sparks reveal a comparably cold surface combustion stage at 1550 K, close to the boiling point of Yb (1466 K), and an intense gas-phase combustion phase with peaks assigned to YbO and YbOH, respectively, at 480 and 530 nm (Figure 3a). Comparing the compositions before and after burning, a significant loss of Yb is revealed (Figure 4b). Particles recovered after spark formation contained approx. 82 at. % copper (metal fraction), matching, for example, with the stable compound Cu_9Yb_2.[43] This confirms that lower-boiling-point Yb is evaporated during the combustion process. Compared to erbium sparks,[18] the green phase is longer, the green color is purer due to reduced underlying black body emission, and the color change is more pronounced since the surface combustion stage is cooler. In the case of Yb−Zn, a rather comparable

https://doi.org/10.1021/acsomega.2c03081
ACS Omega XXXX, XXX, XXX−XXX

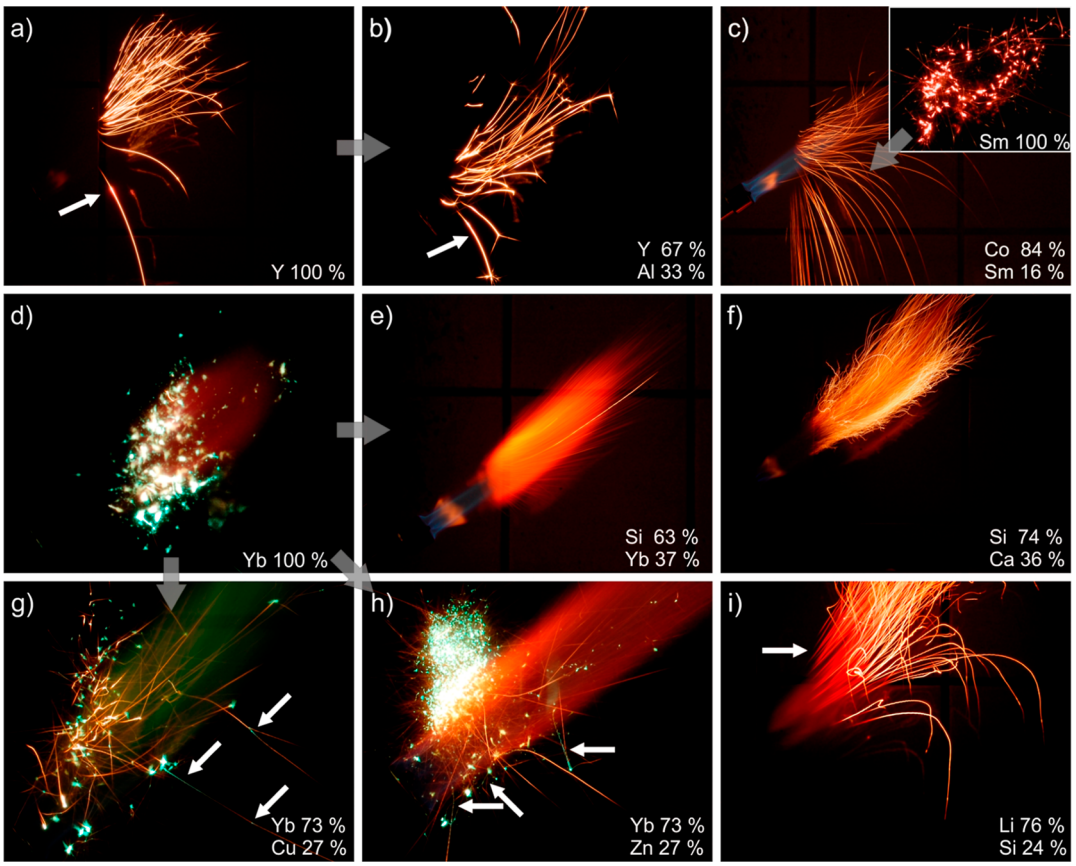

Figure 2. Long-time exposures of sparks based on (a) Y, (b) Y_2Al, (c) $SmCo_5$ (inset: Sm), (d) Yb, (e) Yb_3Si_5, (f) $CaSi_2$, (g) eutectic Yb−Cu, (h) eutectic Yb−Zn, and (i) "Li_3Si" (a mixture of Zintl phases) powder.

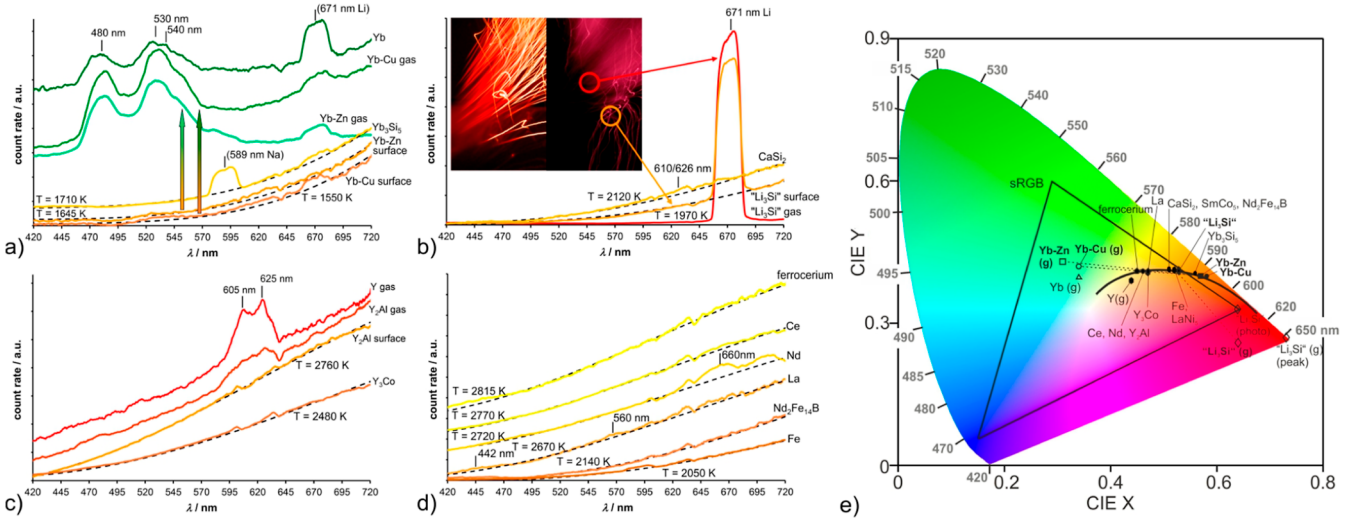

Figure 3. Emission spectra of sparks from (a) Yb and Yb-containing alloys, (b) "Li_3Si" and $CaSi_2$, (c) Y and Y-containing alloys, and (d) Fe, La, Ce, Nd, $Nd_2Fe_{14}B$, and ferrocerium. If appropriate, vapor-phase and surface combustion phases are denoted accordingly. Black body fits are represented by a dashed black line. (e) CIE 1391 chromaticity diagram of spark colors derived from the emission spectra. The black triangle represents the sRGB color space, the black curve represents the black body emitters in the range from 800−4200 K, and the dashed lines connect the colors of the same alloys corresponding to vapor-phase and surface combustion.

appearance is observed. The fraction of long sparks is reduced, and a considerable amount burns with short flashes comparable to that of pure Yb (Figure 2h), which is explained by the low boiling point of Zn. Owing to the low boiling point of both metals, we were not able to recover the burned material. Fortunately, several sparks still show a long golden and green stage, albeit shorter than in the case of Yb−Cu.

The spark temperature of the golden stage (1645 K) and the emission spectrum of the green stage (Figure 3a) are comparable to those of Yb−Cu. Overall, Yb−Cu is a more

https://doi.org/10.1021/acsomega.2c03081
ACS Omega XXXX, XXX, XXX−XXX

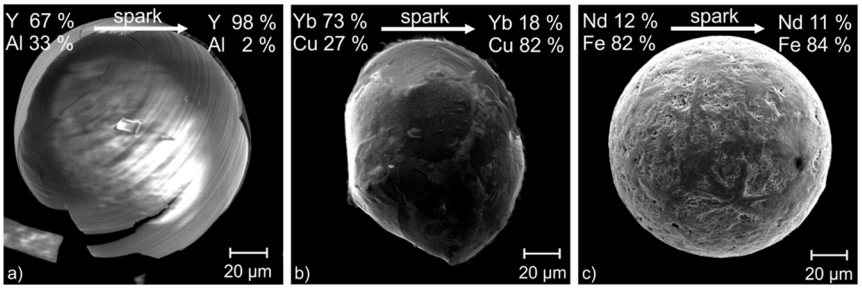

Figure 4. SEM images of particles recovered after burning from (a) Y_2Al, (b) Yb−Cu eutectic alloy, and (c) $Nd_2Fe_{14}B$. Metal ratios (given in atom %) have been obtained by EDX measurements.

promising candidate due to longer sparks, which is as expected according to the high boiling point of Cu.

To cross-check the results of alternating surface and vapor-phase combustion for bimetallic alloys, lithium silicide was investigated as an additional material. Although of purely academic interest due to the high reactivity, lithium silicides are an interesting candidate since they are stable at various Li/Si ratios, Li provides intense atomic emission at 671 nm,[27] and has a low boiling point of 1342 °C. Here, a mixture of Zintl phases with the average composition of "Li_3Si" (Li_3Si itself is not a stable Zintl phase) was chosen, that is, 76 at. % Li, which matches well with the alloys discussed before.[47,48] Indeed, "Li_3Si" forms color-changing sparks with a deep red (3−4 cm) stage and bright golden (3−16 cm) stage (Figure 2i). According to the emission spectra (Figure 3b), the first stage is based on the emission peak from Li at 671 nm, while the second stage reveals black body emission at 1970 K. The NIR image cutting all wavelength <800 nm reveals only the second stage to be visible (see the inset in Figure 3b), which matches with the red phase being basically atomic emission with only weak underlying black body emission. This may be explained by the cooling of the spark by evaporating lithium and explains the bright red visual appearance of the first stage. After Li is consumed, the spark continues as a glowing silicon particle. The recovered particles represent a smooth, glassy appearance, as expected for molten SiO_2 (see Figure S21 of the Supporting Information).

Unfortunately, Li is not detected by EDX, and consequently, the absence of Li in the oxidation product could not be confirmed further. Based on the results of "Li_3Si", the stable Zintl phase $CaSi_2$ was investigated, too. Calcium disilicide is far more stable than lithium silicide and is occasionally used in pyrotechnic compositions despite its reactivity against moisture.[50−52] The sparks obtained from $CaSi_2$ represent a bright golden and nested appearance (Figure 2f). The color reminds more of bright iron sparks, while the trajectory of the sparks is comparable to that of charcoal sparks, which is explainable by the low density of $CaSi_2$ of 2.5 g cm^{-2}. Planck fits of the emission spectra reveal a spark temperature of 2120 K. Only very weak and broad emission bands attributed to CaO at around 610 and 626 nm are recognized on top of the black body emission, which are not expected to influence the color of the spark (Figure 3b).[27] The particles recovered from $CaSi_2$ sparks (see Figure S25 of the Supporting Information) did not reveal a significant change of the elemental ratio. Due to the rather unique appearance and wide availability, stabilized $CaSi_2$ could be kept in mind for spark generation.

To visualize and discuss the color space covered by the sparks described above, emission spectra have been transformed to the corresponding coordinates in the chromaticity diagram (Figure 3e). All black body emitters, that is, all sparks and spark phases based on surface combustion, settle along the black body curve (plotted for 800−4200 K) according to the spark's temperature with only minimal deviations caused by small emission bands, as discussed above. Both lithium silicide as well as the eutectic Yb alloys clearly break the limit of black body radiation. Since the chromaticity diagram is not linear, differences of coordinates in the diagram must be discussed with caution. Still, differences in the same color regions can be compared. For Yb−Cu and Yb−Zn, the distances between the color of the spark during surface combustion and that during vapor-phase combustion have been calculated to be d_{col} = 0.24 and 0.26, respectively. This reflects the slightly shifted color of the Yb−Zn spark and matches with the emission spectra, which reveal the residual underlying black body emission in the case of Yb−Cu, in contrast to Yb−Zn. Compared to erbium (d_{col} = 0.12),[18] the color change is much more pronounced in the case of Yb−Zn as well as for Yb−Cu, and the green phase is significantly purer. The red color of the "Li_3Si" sparks is rather pure, as expected for a single atomic emission line. The CIE coordinates corresponding to the emission spectrum of vapor-phase combustion are slightly shifted from the emission peak toward the blue region and can only be expressed by means of the complementary wavelength C-494 nm in the chromaticity diagram. A possible explanation for the blue shift could be given by the emission from SiO_2. Silicon is likely to be transformed into the gas phase during vapor-phase combustion of "Li_3Si", and SiO_2 shows a series of emission bands in the blue region from 371−474 nm.[27] The emission spectra indeed reveal the background of the vapor-phase combustion stage to be slightly shifted above the corresponding black body/surface combustion stage in the blue region (Figure 3b). Comparing the color change of "Li_3Si" (d_{col} = 0.19) to the white-golden/reddish yttrium spark (d_{col} = 0.02)[18] demonstrates the strong increase in color change, which is explained by a strongly decreased spark temperature and a reduced black body emission in the case of "Li_3Si". Recalculating the RGB values obtained from the red phase of the "Li_3Si" spark in the photographic image taken at a white balance of 6500 K (Figure 2i) into the corresponding CIE coordinates reveals them to be exactly at the right corner of the sRGB triangle plotted in Figure 3e. Consequently, the "Li_3Si" sparks provide "the reddest color" the usual camera, monitor, and printing (CMYK) equipment can visualize, and it is in fact even deeper red than shown in the figures here.

Branching. Besides the spark's color, branching is an important aspect. Typical firework articles such as "sparklers" and the most sophisticated Japanese version, "Senko hanabi",

https://doi.org/10.1021/acsomega.2c03081
ACS Omega XXXX, XXX, XXX−XXX

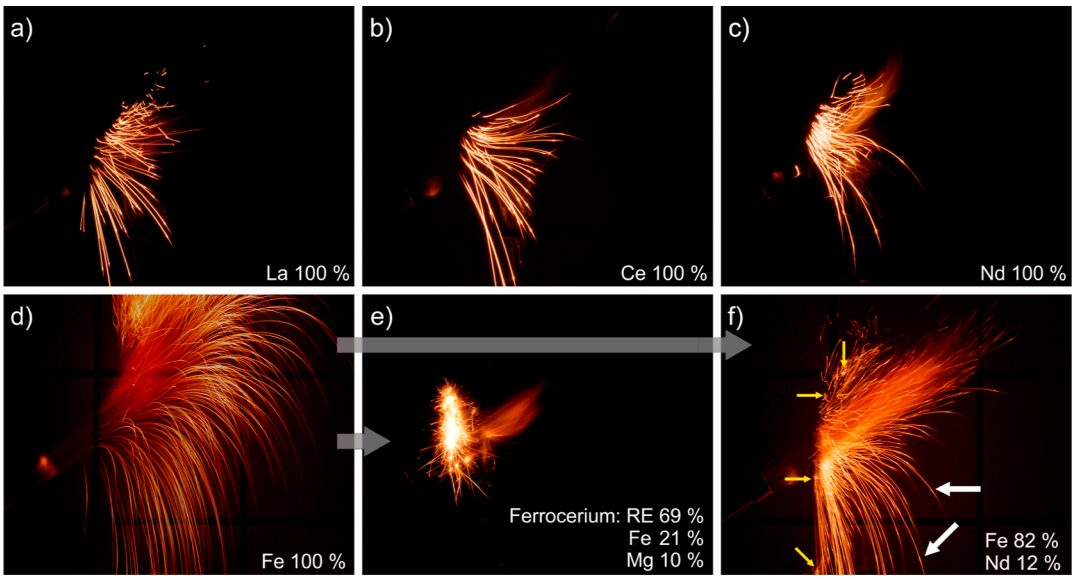

Figure 5. Long-term exposures of sparks based on (a–c) rare-earth elements La, Ce, and Nd as well as (d) iron, (e) ferrocerium (alloy of La, Ce, and other rare-earth elements (RE) with iron in varying compositions), and (f) $Nd_2Fe_{14}B$ powder.

are based on branching sparks. Japanese sparklers have been investigated in detail to visualize and understand the several stages of spark generation and sparks with multiple generations of arborescence (i.e., successive branching events).[53,54] In previous experiments, we observed the strong tendency of pure erbium, yttrium, and thulium to branch, the latter immediately bursting with a crackling sound.[18,21] Ferrocerium, an alloy of iron and mischmetal, which again is an alloy of Ce, La, Nd, and other lanthanides, is well-known as a flint alloy and has a strong tendency to branch.[55] The emissions of CeO, LaO, and NdO are reported to be weak and appear as a faint yellow according to the flame spectra of the corresponding metal salts.[13] Consequently, these elements should be good candidates to control branching without changing the color of sparks. Since pure Ce, La, and Nd had not been investigated previously, spark formation from these elements was analyzed first. All three elements form long sparks (Figure 5a–c and Table 3) with a bright yellowish-white color. Sparks from La appear to be a bit darker and more yellow than the two other materials. As expected, no visible indications for colored phases are observed. In the case of Ce and most prominently in the case of Nd, a thickening of the sparks and an increase in brightness are visible, which may indicate vapor-phase combustion, which could be expected according to the boiling points of 3464 (La), 3443 (Ce), and 3074 (Nd) °C. For Lu (bp. 3402 °C) a very weak vapor-phase combustion stage has been described.[18]

The emission spectra reveal surface combustion and black body emission in all three cases with spark temperatures of 2669 (La), 2770 (Ce), and 2718 (Nd) K. In good agreement with its lowest boiling point, only in the case of Nd was a noteworthy emission band from NdO at around 660 nm observed (Figure 3d).[27] Still, the emission band is weak and hardly affects the color. Emission bands from LaO at around 442 and 560 nm are barely distinguishable from the black body emission. Fortunately, in all three cases, branching of the sparks was observed. Branching was most prominent in the case of lower-boiling-point Nd, while in the case of La and Ce, frequently, an intensity jump but not a successful branching event is observed (Figure 5a–c).

Pure Fe sparks, free of carbon, do not branch (Figure 5d), have a rather low spark temperature of 2054 K, and showed solely surface combustion (Figure 3d). In contrast, the rare-earth iron alloy ferrocerium branched immediately after contact with the flame, as expected (Figure 3e). The chemical composition of the technical alloy was inhomogeneous. A composition of 69 at. % rare-earth metals, 21 at. % Fe, and 10 at. % additional Mg was determined in average. Mg is added to ferrocerium to increase the heat of combustion (and, as a consequence, the spark temperature).[55] Indeed, a spark temperature of 2815 K was derived from the Planck fit of the emission spectrum, clearly above the spark temperature of pure La, Ce, and Nd. The emission spectrum did not reveal a significant contribution from rare-earth monoxide emission bands (Figure 3d). In agreement with the observations described above, magnesium was found to be absent in the particles recovered after spark formation. Apparently, the low-boiling-point element (bp. 1110 °C)[28] is evaporated to a significant fraction during the burning process. The SEM image of the burned ferrocerium particles revealed several craters (see Figure S26 of the Supporting Information), which is in agreement with the strong tendency to burst. Based on the theories of branching discussed above, (i) gas release from metal–gas phases, (ii) low-boiling-point magnesium, and finally (iii) the brittle structure of the material, with phase-separated fractions of Ce_2Fe_{17} and $CeFe_2$,[55] can explain the tendency to branch. Obviously, ferrocerium is far too pyrophoric and branching occurs too fast to be applicable for pyrotechnic spark generation. A commercial neodymium–iron alloy with approx. 12 at. % of Nd was investigated next. Nd–Fe alloys are produced by the ton to form permanent magnets. 1 wt. % of boron is commonly added to achieve the stable phase $Nd_2Fe_{14}B$. Sparks from $Nd_2Fe_{14}B$ appear brighter than those from pure iron (Figure 5f), which is confirmed by the increased spark temperature of 2142 K. The emission spectrum (Figure 3d) does not show any indication for vapor-phase combustion in the form of emission bands from NdO at 660 nm. In accordance with solely surface combustion being observed, the burned particles recovered after spark formation (Figure 4c) did not reveal a change in the metal ratio before

https://doi.org/10.1021/acsomega.2c03081
ACS Omega XXXX, XXX, XXX–XXX

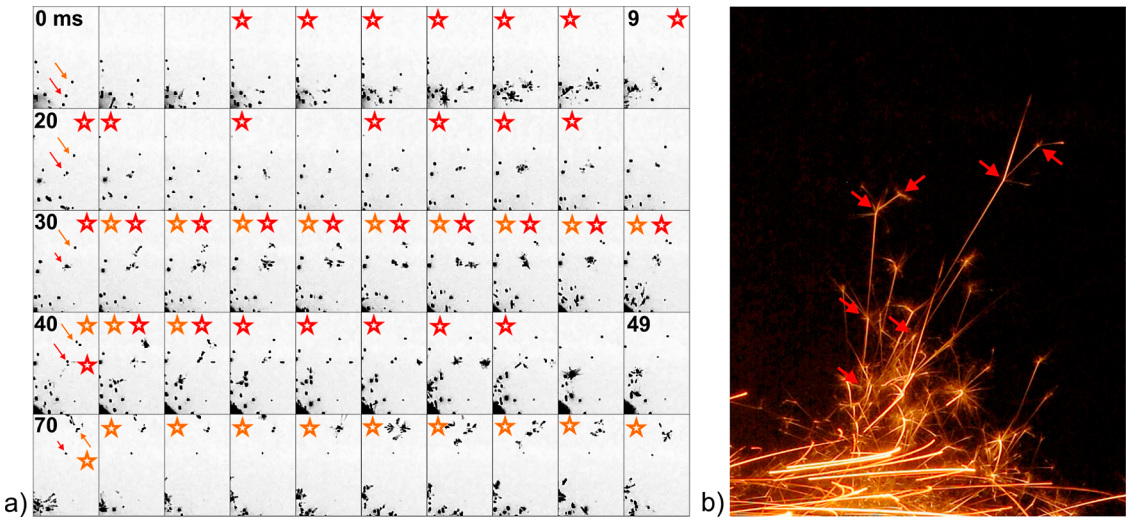

Figure 6. Branching of sparks based on $Nd_2Fe_{14}B$ emitted from an ammonium perchlorate/nitrocellulose-based fountain. (a) Snapshots of two isolated sparks captured by high-speed imaging every 1 ms. Branching events are indicated by a colored star. Weak branching events have been omitted. (b) Visible image taken with an exposure time of 65 ms, presenting up to four successive branching events.

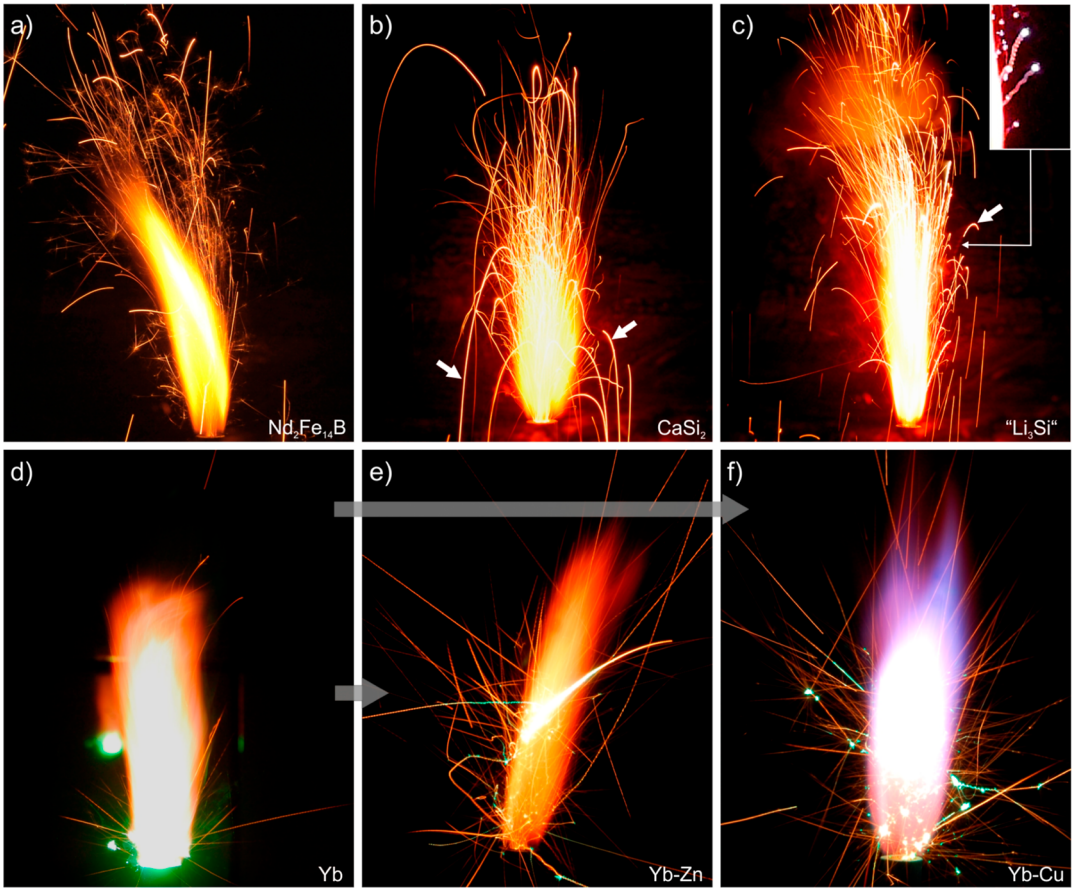

Figure 7. Photographic images (exposure time 65 ms) of ammonium perchlorate/nitrocellulose-based fountains emitting sparks from (a) $Nd_2Fe_{14}B$, (b) $CaSi_2$, (c) "Li_3Si" (inset: snapshot of high-speed imaging video at 1000 fps), (d) Yb, (e) Yb−Zn, and (f) Yb−Cu powder.

and after burning. Fortunately, the sparks are occasionally terminated by a branching event (see the four branched sparks in Figure 5f). The most important aspect is revealed by a close look at the spark's brightness. In contrast to the iron sparks, which slowly fade out, in the case of sparks obtained from $Nd_2Fe_{14}B$, an increase in brightness is observed at the end of each spark. This intensity jump is typical for an almost occurring branching event, as described above. The tendency to promote branching with alloys containing a fraction of rare-earth elements is confirmed by Y_2Al (Figure 2b), although aluminum sparks usually do not branch.[11] Y_3Co showed branching, too, and only the sparks from $SmCo_5$ and $LaNi_5$ powder (see Figures S2, S24, and S29 of the Supporting

https://doi.org/10.1021/acsomega.2c03081
ACS Omega XXXX, XXX, XXX−XXX

Information for an investigation of $LaNi_5$ sparks) showed neither branching nor an intensity jump at the end.

As observed earlier, branching is more pronounced if the particles are emitted from a pyrotechnic composition instead of ignition from short contact with a gas flame.[18,21] Here, a selection of promising candidates for branching, as well as colored spark generation, have been added as a spark-generating additive to an ammonium perchlorate/nitrocellulose (21:79 wt. %)-based propellant for smokeless fountains. The composition containing additional 12.5 wt. % of metal powders has been filled loosely in tubes with a 1 cm inner diameter. The burn rate was determined to be approx. 1.5−1.6 mm s^{-1}. The composition based on ferrocerium, of purely academic interest due the the highly pyrophoric nature, emits immediately branching sparks that hardly reach out of the tube (Figure S32 of the Supporting Information). Probably due to sparks penetrating the composition and the pyrophoricity of ferrocerium, the burn rate is increased to 2.5 mm s^{-1}. In the case of $Nd_2Fe_{14}B$, a very attractive continuous branching of the sparks is observed. In photographic images, at least four stages of arborescence are revealed (Figure 6b). The sparks have been analyzed further by high-speed imaging with a frame rate of 1000 fps. Figure 6a presents selected snapshots of a cutout from the video file focusing on two isolated sparks marked with colored arrows. The sparks start at the bottom of the snapshot at 0 ms and slowly proceed to the top (79 ms). During this time, both particles repeatedly branch into several fragments, while each mother particle continues its path. Snapshots with visible branching of each spark have been highlighted with a star in the corresponding color. Snapshots with additional weak branching events have been omitted in the representation. Overall, both sparks continuously branch over a time of approx. 50 ms. The whole extent of spark generation is represented in the supplementary slow-motion video file of the fountain with sparks from $Nd_2Fe_{14}B$.

For comparison, a commercial ice star fountain (bottle sparkler) is shown in a supplementary video and a photographic image (Figure S33 of the Supporting Information). The stages of branching are significantly reduced in comparison to the fountain containing $Nd_2Fe_{14}B$. Sparks are terminated by a single branching event in most cases, and ongoing repeated branching for several tens of milliseconds is not observed.

With regard to colored sparks, the same pyrotechnic composition with "Li_3Si" and $CaSi_2$ as the spark-generating additive has been investigated first. "Li_3Si" is again only of academic interest due to its high reactivity. The burning rate in the presence of "Li_3Si" is increased to 2.0 mm s^{-1}. Unfortunately, the bright red first phase of the "Li_3Si" sparks described above is nearly invisible in the case of the sparks ejected from the tube (Figure 7c). Possibly, highly reactive "Li_3Si" reacts immediately with the composition, and the red burning phase did not reach out of the tube. The majority of sparks are bright yellowish, in agreement with the surface combustion of Si, as discussed above. Some isolated sparks reveal a bright reddish-white appearance, which might be affected by the Li content. This assumption is backed by the smoke trail of the sparks (see the inset of Figure 7c), which could indicate gas-phase combustion of Li or sublimating lithium oxide. The twisted structure of the smoke trail indicates inhomogeneous burning of the particles. The fountain based on $CaSi_2$ reflects the thin, nested appearance of the sparks obtained from the lightweight fine powder (Figure 7b). Some isolated thicker sparks reveal an orange appearance, which could indicate a contribution from CaO emission, which is very weak, as discussed above. The unique appearance of the sparks, again somehow between iron and charcoal, together with the broad availability and low toxicity of calcium disilicide makes $CaSi_2$ a candidate to keep in mind for pyrotechnic spark generation, although the limited stability against humidity restricts its possible applications. The most promising sparks in terms of exotic colors are obtained from the eutectic Yb alloys. While in the case of Yb, the "sparks" do not reach out of the tube and the composition burns with bright green flashes (Figure 7d), in the cases of both Yb−Zn and Yb−Cu, long green spark phases are observed (Figure 7e,f). In both cases, dark golden sparks with intense green segments dominate the visual appearance. Usually, the green phase is the first phase, which slowly fades out into the golden phase. In the case of Yb−Cu, the golden phase is repeatedly interrupted by a shorter green phase (Figure 7f). Occasionally, the green phase is accompanied by a branching event. Some sparks reflect a rotating movement of the burning particle, visible as a rapidly alternating green and golden trajectory. This indicates inhomogeneous combustion on the same particle and preferred gas release on one side of the particle, as observed in the case of "Li_3Si". It is noteworthy to point out the blue flame color of the composition in the presence of the Yb−Cu alloy (Figure 7f), in contrast to the greenish color of the gas flame in contact with the same alloy (Figure 2g). The blue color is readily explained by the presence of chloride (from ammonium perchlorate, here), an oxygen-deficient combustion, and a low flame temperature, all together favoring CuCl as the emitting species.[2,12,56] The oxygen balance of the ammonium perchlorate/nitrocellulose composition based on weakly nitrated cellulose with a nitrogen content of 9.6%, that is, with approx. 1.6 out of 3 possible nitrate ester groups per glucose unit, is $\Omega = -35.7\%$, neglecting the additional metal content. The color is in agreement with the blue strobes presented by Jennings-White based on the Cu−Al (1:1) alloy, ammonium perchlorate, and guanidine nitrate and the further blue strobes discussed by Klapötke.[57,58]

Toxicity, Stability, and Availability. The application of rare-earth elements in fireworks needs to be discussed critically due to their limited stability, rather high costs, and possible toxicity. The spark's appearance presented here is only visible on an extremely short distance. None of the effects described above is visible on the distance of aerial shells, comets, or mines. In contrast, hand-held sparklers, indoor stage pyrotechnics, and similar effects might be a potential target. From the alloys discussed above, the most interesting and realistic candidates are $Nd_2Fe_{14}B$, in view of the continuously branching sparklers, and the eutectic Yb−Cu alloy, in view of the unconventionally colored sparks. Concerning the stability, both are fortunately stable. Yb has been described as one of the most stable lanthanides.[14] The Yb−Cu alloy, in contrast to the Yb−Zn alloy, retained its silvery gloss for months without any indication of oxidation at ambient conditions (see Figure S34 of the Supporting Information), and the usual coating protocols are likely to be transferable to both alloys. Some investigations have been carried out concerning the stability, friction sensitivity, impact sensitivity, flame sensitivity, and electrostatic sensitivity of rare-earth metal-containing alloys for civilian and military pyrotechnic applications.[59,60] Compositions with alloys of rare-earth metals/mischmetal with zinc and

https://doi.org/10.1021/acsomega.2c03081
ACS Omega XXXX, XXX, XXX−XXX

copper have shown to be comparable in all these categories to the same composition based on magnalium.[59]

Concerning the toxicity, inhalation of rare-earth oxide dust can be seen as the most considerable risk. In general, almost all metal oxides such as aluminum or zinc oxide have pulmonary effects if inhaled chronically, still they are considered to be harmless even in indoor pyrotechnic materials.[61,62] For long-term inhalation of rare-earth fumes, for example, in the case of a smelter after 18 month of exposition, pneumoconiosis has been confirmed, which is not surprising compared to other metal oxide dusts.[63] By intratracheal instillation in rat lungs, the pulmonary toxicity of YCl_3 was evaluated to be 3 times higher than that of ZnO,[64] but a soluble rare-earth halogenide must be considered more harmful than unsoluble rare-earth oxides.[65] A detailed investigation concerning the inhalation of Gd_2O_3 dust from mice came to the conclusion that "even at heavy exposure levels, Gd_2O_3 ranks as a low-grade pulmonary irritant" with "very little tendency to pulmonary fibrosis".[65] Overall, and to the best of our knowledge based on these investigations, rare-earth oxide dusts emitted from pyrotechnic articles are not a critical aspect and can be considered comparable to other metal oxides.

Finally, the price of rare-earth metals is rather high. For most of the rare-earth metals, a price between 10 and 100 EUR/kg has been documented over the last decade, fluctuating with export restrictions and discovery of new deposits.[66] For the most interesting alloys discussed here, $Nd_2Fe_{14}B$ and Yb−Cu, a recent price of 154,000 yuan/ton, that is, 21 EUR/kg for the alloy $Nd_2Fe_{14}B$ and 15 EUR/kg for the pure Yb metal, is given.[67,68] Assuming a net explosive content (NEC) of 1 g per handheld sparkler with 50% metal content, the price of a $Nd_2Fe_{14}B$-based sparkler would increase by 1 €-cent/sparkler or 10−20 €-cent/box of sparklers. Compared to a typical end-market price of 50 €-cent/box, this is still significant yet not unrealistic. Stage pyrotechnics is usually on a rather high price segment with typical selling prices of 10 EUR/small stage jet or airburst. Assuming approx. 10 g of NEC, the price would increase by approx. 10 €-cent/pcs if based on Yb−Cu alloys (taking the pure metal price of Yb into account), which would not be a limiting factor.

CONCLUSIONS

Binary metal alloys pave the way to sparks with colors beyond the limit of black body radiation. Sparks based on a eutectic Yb−Cu alloy (73 at. % Yb) or a eutectic Yb−Zn alloy (73 at. % Yb) show a unique appearance with golden and intense green stages, sparks from the stable compound Y_2Al: (67 at. % Y) reveal a short red stage, and sparks obtained from the mixture of Zintl phases "Li_3Si" (76 at. % Li) reveal a deep red stage before they fade into bright black body radiation. In general, a content of >65 at. % of the usually low-boiling-point coloring agents seems to be necessary to achieve an element-specific colored spark stage. Sparks from Yb−Cu/Yb−Zn and "Li_3Si" reveal the strongest color change of sparks reported so far, clearly switching the visible color across the chromaticity diagram. Besides the color, branching of sparks can be controlled by the rare-earth metal content (Y_2Al, Y_3Co, ferrocerium, and $Nd_2Fe_{14}B$). $Nd_2Fe_{14}B$ sparks show repetitive branching events with multiple stages. $Nd_2Fe_{14}B$ and the eutectic Yb−Cu alloy as well as $CaSi_2$ are the most realistic candidates for an application as exotic sparks-generating fuels due to their stability, low toxicity, accessibility, and visual appearance of sparks. The upcoming work focuses on an investigation of selected pyrotechnic compositions for handheld sparklers and stage gerbs based on these alloys.

METHODS

Caution! The rare-earth metal powders and rare-earth metal-containing alloys investigated here are highly reactive, and freshly prepared powders are likely to be pyrophoric at air. Formulations given are meant for research purposes only and may be unstable. Mixtures containing ammonium perchlorate and nitrocellulose are potential explosives and should be handled with care. Rare-earth metal-containing formulations emit bright (UV) light, and appropriate eye protection is required. Experiments with nickel- and cobalt-containing powders require a well-ventilated hood.

Lanthanum (99.9%), cerium (99.9%), neodymium (99.9%), ytterbium (99.95%), yttrium (99.95%), erbium (99.9%), and samarium (99.95%) were obtained as blocks from Onyxmet and have been rasped to powders using a diamond-coated rasp in a glovebox. Amorphous boron (99.9%, Onyxmet), copper (99.9%, Onyxmet), zinc (99.8%, Onyxmet), and iron (99%, Sigma-Aldrich), as well as "Li_3Si" (Gelest), Yb_3Si_5 (Alfa Aesar), $CaSi_2$ (Werth-Metall), and $LaNi_5$ (Alfa Aesar), have been obtained as powders and used as received. Y_3Co (Alfa Aesar), Y_2Al (Alfa Aesar), and $Nd_2Fe_{14}B$ (1 wt. % B, Alfa-Aesar) have been obtained as lumps, ferrocerium (Polymet) was obtained as rod, and they have been rasped to powders using a diamond-coated rasp in a glovebox. $SmCo_5$ (Sigma-Aldrich) has been obtained as a magnetized disk, demagnetized at 900 °C under vacuum in a sealed quartz tube, and subsequently rasped to a powder. Stabilized and plasticized nitrocellulose (Pyroflash Spezialeffekte) with a nitrogen content of 9.6% was ground to a powder with a mortar and pestle. Ammonium perchlorate (Fluka) has been used as received. Particle sizes of all metal powders were estimated by laser scanning microscopy (Keyence VK-X200). SEM images have been obtained on an EVO MA10 (Zeiss) scanning electron microscope. The elemental compositions of metal particles before and metal oxide particles after spark formation have been determined using an EDX unit (Bruker XFlash 6/30) integrated into the scanning electron microscope. Accelerating voltages have been set according to the corresponding X-ray lines of the elements. Long-time exposures (shutter speed of 1 s) were obtained using a digital camera (Nikon D40) at a white balance of 6500 K. Due to the strongly differing brightness of the sparks, varying aperture settings were used. Images were adjusted in overall brightness. No color corrections or tone adjustments were applied. An IR cut filter at 850 nm has been used to visualize the NIR region from 800−1100 nm. High frame rate videos have been captured at 960 fps using an Exmor RS IMX563 CMOS sensor. Emission spectrometric measurements have been recorded using an AvaSpec-2048-USB2 spectrometer (Avantes) equipped with a 600 μm multimode glass fiber (Avantes FCB-UV/IR600-2-ME). The setup has been calibrated with an incandescent tungsten lamp at 2715 K. All spectra have been recorded with an integration time of 1 ms, and spectra have been recorded every 8 ms. Planck curve fits have been prepared using OriginPro 2021. Chromaticity diagrams according to the CIE 1931 standard (Commission Internationale de l'éclairage) have been prepared using GoCIE v2 with the CIE standard illuminant D65 as the white reference point.[69] All powders have been passed into the center of the invisible gas flame of a Teclu burner operated with methane through an aluminum tube from a distance of 20 cm.

https://doi.org/10.1021/acsomega.2c03081
ACS Omega XXXX, XXX, XXX−XXX

Alloys. Eutectic Yb alloys have been prepared from the elements according to a procedure given in the literature.[44] The appropriate amount (total mass of 5 g) of metal powders has been weighed into quartz glass tubes (Ø 20 mm i.d) in a glovebox. Tubes have been evacuated and sealed using an oxyhydrogen torch. For Yb−Cu, a graphite crucible (Ø 20 mm o.d., LLF) has been inserted into the glass tube. The sealed tubes have been heated above the melting point of each component (Yb−Zn: 900 °C and Yb−Cu: 1100 °C) for 5 h in a muffle furnace (Nabertherm L 9/13 B150). Tubes have been opened in a glovebox, and the alloy was rasped to a powder using a diamond-coated rasp.

Smokeless Fountain. A paper tube (5 cm length, 1 cm inner diameter, and 2.5 mm wall thickness) has been plugged with bentonite, which has been strongly compactified using a plunger to up to 2 cm from the top. Plastified nitrocellulose ground to a fine powder (1.10 g), ammonium perchlorate powder (0.30 g), and metal powder (0.20 g) were mixed by repeated shifting on a paper sheet. The resulting mixture was inserted into the upper compartment of the paper tube until it was flush with the ending of the tube. The burn time is 12−13 s.

■ ASSOCIATED CONTENT

Supporting Information

The Supporting Information is available free of charge at https://pubs.acs.org/doi/10.1021/acsomega.2c03081.

Additional emission spectra, SEM images, photographic images of sparks, and light microscopic images of alloys and metal powders (PDF)

Slow-motion video sequence (1/160× speed) of a smokeless fountain emitting continuously branching sparks from Nd2Fe14B (MP4)

Slow-motion video sequence (1/160× speed) of a commercial ice star fountain (MP4)

■ AUTHOR INFORMATION

Corresponding Author

Eike G. Hübner − *Institute of Organic Chemistry, Clausthal University of Technology, DE-38678 Clausthal-Zellerfeld, Germany; Fiber Optical Sensor Systems, Fraunhofer Heinrich Hertz Institute, HHI, DE-38640 Goslar, Germany;* orcid.org/0000-0003-2104-9615; Email: eike.huebner@tu-clausthal.de

Authors

Philipp Memmel − *Institute of Organic Chemistry, Clausthal University of Technology, DE-38678 Clausthal-Zellerfeld, Germany; Fiber Optical Sensor Systems, Fraunhofer Heinrich Hertz Institute, HHI, DE-38640 Goslar, Germany*

Felix Lederle − *Fiber Optical Sensor Systems, Fraunhofer Heinrich Hertz Institute, HHI, DE-38640 Goslar, Germany;* orcid.org/0000-0002-7369-7449

Martin Söftje − *Fiber Optical Sensor Systems, Fraunhofer Heinrich Hertz Institute, HHI, DE-38640 Goslar, Germany; EST Research Centre Energy Storage Technologies, Clausthal University of Technology, DE-38640 Goslar, Germany;* orcid.org/0000-0002-6794-0748

Jannis Koch − *Fiber Optical Sensor Systems, Fraunhofer Heinrich Hertz Institute, HHI, DE-38640 Goslar, Germany*

Mingji Li − *Fiber Optical Sensor Systems, Fraunhofer Heinrich Hertz Institute, HHI, DE-38640 Goslar, Germany*

Wolfgang Schade − *Fiber Optical Sensor Systems, Fraunhofer Heinrich Hertz Institute, HHI, DE-38640 Goslar, Germany; Institute of Energy Research and Physical Technologies, Clausthal University of Technology, DE-38640 Goslar, Germany*

Complete contact information is available at: https://pubs.acs.org/10.1021/acsomega.2c03081

Author Contributions

The manuscript was written through contributions of all authors. All authors have given approval to the final version of the manuscript.

Notes

The authors declare no competing financial interest.

■ ACKNOWLEDGMENTS

We sincerely thank Roland Zain for the preparation of vacuum-sealed quartz glass tubes. We gratefully acknowledge the financial support from the Open Access Publishing Fund of the Clausthal University of Technology.

■ DEDICATION

Dedicated to John A. Conkling † Dec. 18, 2021 for his life's work on pyrotechnics.

■ ABBREVIATIONS

bb, black body; CIE, Commission Internationale de l'éclairage; EDX, energy-dispersive X-ray spectroscopy; ICP-OES, inductively coupled plasma—optical emission spectrometry; NEC, net explosive content; NIR, near-infrared;; PTFE, polytetrafluoroethylene; RE, rare-earth; SEM, scanning electron microscopy; Sp, spectral; sRGB, standard red green blue color space; UV, ultraviolet; WL, wavelength

■ REFERENCES

(1) Kosanke, B. J.; Kosanke, K. L.; Jennings-White, C. Pyrotechnic Spark Generation. In *Pyrotechnic Reference Series No. 4: Pyrotechnic Chemistry*; Kosanke, K. L., Kosanke, B. J., Sturman, B., Shimizu, T., Wilson, M. A., von Maltitz, I., Hancox, R. J., Kubota, N., Jennings-White, C., Chapman, D., Dillehay, D. R., Smith, T., Podlesak, M., Eds.; Journal of Pyrotechnics, Inc.: Whitewater, 2004, pp 1−14. Chapter 13.

(2) Shimizu, T. *Fireworks The Art, Science and Technique*, 3rd ed.; Pyrotechnica Publications: Austin, 1981.

(3) Conkling, J. A. *Chemistry of Pyrotechnics*; Marcel Dekker, Inc.: New York, 1985.

(4) Russell, M. S. *The Chemistry of Fireworks*, 2nd ed.; The Royal Society of Chemistry: Cambridge, 2009.

(5) Jennings-White, C. Some Esoteric Firework Materials. *Pyrotechnica* **1990**, *XIII*, 26−32.

(6) Shoshin, Y. L.; Mudryy, R. S.; Dreizin, E. L. Preparation and Characterization of Energetic Al-Mg Mechanical Alloy Powders. *Combust. Flame* **2002**, *128*, 259−269.

(7) Schoenitz, M.; Dreizin, E. Oxidation Processes and Phase Changes in Metastable Al−Mg Alloys. *J. Propul. Power* **2004**, *20*, 1064−1068.

(8) Ouyang, D.; Pan, G.; Guan, H.; Zhu, C.; Chen, X. Effect of Different Additives on the Thermal Properties and Combustion Characteristics of Pyrotechnic Mixtures Containing the $KClO_4$/Mg−Al Alloy. *Thermochim. Acta* **2011**, *513*, 119−123.

(9) Han, B.; Gnanaprakash, K.; Park, Y.; Yoh, J. J. Understanding the Effects of Hygrothermal Aging on Thermo-Chemical Behaviour of Zr-Ni Based Pyrotechnic Delay Composition. *Fuel* **2020**, *281*, 118776.

(10) Zhao, W.; Jiao, Q.; Chen, P.; Yan, S.; Zhu, Y.; Zhang, B.; Zeng, X.; Liu, D.; Ou, Y.; Wang, F. Synergetic energetic kinetics of Mg-Zn alloys and pyrotechnics. *Combust. Flame* **2022**, *240*, 112000.
(11) Kosanke, K. L.; Kosanke, B. J.; Sturman, B. T.; Winokur, R. M. Spark Branching. In *Pyrotechnic Reference Series No. 5: Encyclopedic Dictionary of Pyrotechnics Part 3*; Kosanke, K. L., Kosanke, B. J., Sturman, B. T., Winokur, R. M., Eds.; PyroLabs, Inc.: Whitewater, 2012, p 1044.
(12) Kosanke, K. L.; Kosanke, B. J. The Chemistry of Colored Flame. In *Pyrotechnic Reference Series No. 4: Pyrotechnic Chemistry*; Kosanke, K. L., Kosanke, B. J., Sturman, B., Shimizu, T., Wilson, M. A., von Maltitz, I., Hancox, R. J., Kubota, N., Jennings-White, C., Chapman, D., Dillehay, D. R., Smith, T., Podlesak, M., Eds.; Journal of Pyrotechnics, Inc.: Whitewater, 2004, pp 1−52. Chapter 9.
(13) Sturman, B. T. The Rare Earths as Possible Flame Color Agents. *J. Pyrotech.* **1999**, 57−61.
(14) Koch, E.-C.; Weiser, V.; Roth, E.; Kelzenberg, S. Consideration of Some 4f-Metals as New Flare Fuels-Europium, Samarium, Thulium and Ytterbium. In *Energetic Materials: Modelling, Simulation and Characterisation of Pyrotechnics, Propellants and Explosives, 42nd International Annual Conference of ICT*; Fraunhofer ICT: Karlsruhe, 2011, pp 1−11. Chapter 1.
(15) Koch, E.-C.; Weiser, V.; Roth, E.; Knapp, S.; van Lingen, J.; Moorhoff, J. Metal−Fluorocarbon Pyrolants. XV: Combustion of two Ytterbium−Halocarbon Formulations. *J. Pyrotech.* **2012**, *31*, 51−57.
(16) Koch, E.-C.; Weiser, V.; Roth, E.; Knapp, S.; Kelzenberg, S. Combustion of Ytterbium Metal. *Propellants, Explos., Pyrotech.* **2012**, *37*, 9−11.
(17) Roth, E.; Knapp, S.; Raab, A.; Weiser, V.; Koch, E.-C. Emission Spectroscopy of Some 4f-Metal Flames. *Energetic Materials: Characterization and Modeling of Ignition Process, Reaction Behavior and Performance, 44th International Annual Conference of ICT*; Fraunhofer ICT: Karlsruhe, 2013, pp 1−10. Chapter 68.
(18) Lederle, F.; Koch, J.; Schade, W.; Hübner, E. G. Color-Changing Sparks from Rare Earth Metal Powders. *Z. Anorg. Allg. Chem.* **2020**, *646*, 37−46.
(19) Steinberg, T. A.; Wilson, D. B.; Benz, F. The Combustion Phase of Burning Metals. *Combust. Flame* **1992**, *91*, 200−208.
(20) Gordon, D. A. Combustion Characteristics of Metal Particles. In *Solid Propellant Rocket Research, Progress in Astronautics and Aeronautics*; Summerfield, M., Ed.; Academic Press: New York, 1960, pp 271−278.
(21) Lederle, F.; Koch, J.; Hübner, E. G. Colored Sparks. *Eur. J. Inorg. Chem.* **2019**, *2019*, 928−937.
(22) Dreizin, E. L. Phase Changes in Metal Combustion. *Prog. Energy Combust. Sci.* **2000**, *26*, 57−78.
(23) Guillen, A.; Goh, F.; Andre, J.; Barral, A.; Brochet, C.; Louis, Q.; Guillet, T. From the Microstructure of Steels to the Explosion of Sparks. *Em. Sci* **2019**, *3*, 2.
(24) Zepper, E. T.; Pantoya, M. L.; Bhattacharya, S.; Marston, J. O.; Neuber, A. A.; Heaps, R. J. Peering through the Flames: Imaging Techniques for Reacting Aluminum Powders. *Appl. Opt.* **2017**, *56*, 2535−2541.
(25) Miedema, A. R. On the Heat of Formation of Solid Alloys. II. *J. Less Common. Met.* **1976**, *46*, 67−83.
(26) Debski, A.; Debski, R.; Gasior, W. New Features of Entall Database: Comparison of Experimental and Model Formation Enthalpies. *Arch. Metall. Mater.* **2014**, *59*, 1337−1343.
(27) Pearse, R. W. B.; Gaydon, A. G. *The Identification of Molecular Spectra*, 4th ed.; Chapman and Hall: London, 1976.
(28) Zhang, Y.; Evans, J. R. G.; Yang, S. Corrected Values for Boiling Points and Enthalpies of Vaporization of Elements in Handbooks. *J. Chem. Eng. Data* **2011**, *56*, 328−337.
(29) *CRC Handbook of Chemistry and Physics*, 84th ed.; Lide, D. R., Ed.; CRC Press LLC: Boca Raton, 2004.
(30) *JANAF Thermochemical Tables*, Vol. *14*, 3rd ed.; Lide, D. R., Ed.; ACS and AIP: New York, 1985; p 1190.
(31) Lewis, R. J., Sr. *Sax's Dangerous Properties of Industrial Materials*, 11th ed.; John Wiley & Sons, Inc.: Hoboken, 2004.
(32) Konar, B.; Van Ende, M.-A.; Jung, I.-H. Critical Evaluation and Thermodynamic Optimization of the Li-O, and Li_2O-SiO_2 Systems. *J. Eur. Ceram* **2017**, *37*, 2189−2207.
(33) Jaeger, F. M.; van Klooster, H. S. Studies in the Field of Silicate Chemistry. I. Compounds of Lithia with Silica. *Versl. Gewone Vergad. Afd. Natuurkd., K. Ned. Akad. Wet.* **1914**, *22*, 900−923.
(34) Calciumoxid. In *Römpp Chemie Lexikon*, 9th ed.; Falbe, J.; Regitz, M., Eds.; Georg Thieme Verlag: Stuttgart, 1992; p 557.
(35) Benezech, G.; Coutures, J. P.; Foex, M. Estimation des températures d'ébullition des sesquioxydes de lanthanides. *J. Less Common. Met.* **1974**, *38*, 131−136.
(36) Silverman, A.; Morey, G. W.; Rossini, F. D. Data on Chemicals for Ceramic Use. *Natl. Res. Counc. Bull.* **1943**, *107*, 1−94.
(37) Nie, H.; Schoenitz, M.; Dreizin, E. L. Oxidation of Magnesium: Implication for Aging and Ignition. *J. Phys. Chem. C* **2016**, *120*, 974−983.
(38) Nakajima, H.; Nakamura, R. Fabrication of Hollow Nano Particles of Metallic Oxides through Oxidation Process. *Mater. Sci. Forum* **2010**, *638-642*, 67−72.
(39) Moeller, T. The Chemistry of the Lanthanides. In *Comprehensive Inorganic Chemistry*; BailarJr, J. C., Emeléus, H. J., Sir Nyholm, R., Trotman-Dickenson, A. F., Eds.; Pergamon Press: Oxford, 1973.
(40) Xiaowei, Z.; Zhiqiang, W.; Dehong, C.; Zongan, L.; Ruiying, M.; Shihong, Y. Preparation of High Purity Rare Earth Metals of Samarium, Ytterbium and Thulium. *Rare Met. Mater. Eng.* **2016**, *45*, 2793−2797.
(41) Brutti, S.; Balducci, G.; Ciccioli, A.; Gigli, G.; Manfrinetti, P.; Palenzona, A. Thermochemistry of Ytterbium Silicides. *Intermetallics* **2003**, *11*, 1153−1159.
(42) Abbati, I.; Braicovich, L.; Carbone, C.; Nogami, J.; Lindau, I.; Iandelli, I.; Olcese, G.; Palenzona, A. Photoemission Studies of Mixed Valence in Yb_3Si_5, YbSi an Yb_5Si_3: Equivalent Versus Inequivalent Yb Sites. *Solid State Commun.* **1987**, *62*, 35−39.
(43) *ASM Handbook*, Vol. 3: *Alloy Phase Diagrams*, 10th ed.; Baker, H., Ed.; ASM International, Materials Park, Ohio, 1992.
(44) Verbovytskyy, Y.; Gonçalves, A. P. The Yb-Zn-Ga system: Partial Isothermal Section at 400 °C with 0-33.3 at.% Yb. *Intermetallics* **2010**, *18*, 655−665.
(45) Mason, J. T.; Chiotti, P. The Ytterbium-Zinc Phase Diagram. *Trans. Metall. Soc. AIME* **1968**, *242*, 1167−1171.
(46) Iandelli, A.; Palenzona, A. The Ytterbium-Copper System. *J. Less Common. Met.* **1971**, *25*, 333−335.
(47) Dębski, A.; Gąsior, W.; Góral, A. Entha of Formation of Intermetallic Compounds from the Li-Si System. *Intermetallics* **2012**, *26*, 157−161.
(48) Braga, M. H.; Dębski, A.; Gąsior, W. Li−Si Phase Diagram: Enthalpy of Mixing, Thermodynamic Stability, and Coherent Assessment. *J. Alloys Compd.* **2014**, *616*, 581−593.
(49) Brutti, S.; Ciccioli, A.; Balducci, G.; Gigli, G.; Manfrinetti, P.; Napoletano, M. Thermodynamic Stabilities of Intermediate Phases in the Ca−Si system. *J. Alloys Compd.* **2001**, *317-318*, 525−531.
(50) Smit, K. J.; de Yong, L. V.; Hatt, D. J.; Wilson, M. A.; Hancox, R. J. Infrared Emission Spectroscopy of the Combustion of Calcium Silicide Based Compositions. *Proceedings of 3rd Australian Conference on Vibrational Spectroscopy*; University of Melbourne: Melbourne, 1998, p 188.
(51) Koch, E.-C.; Clément, D. Special Materials in Pyrotechnics: VI. Silicon − An Old Fuel with New Perspectives. *Propellants, Explos., Pyrotech.* **2007**, *32*, 205−212.
(52) Rugunanan, R. A.; Brown, M. E. Combustion of Binary and Ternary Silicon/Oxidant Pyrotechnic Systems, Part II: Binary Systems with Sb_2O_3 and KNO_3 as Oxidants. *Combust. Sci. Technol.* **1993**, *95*, 101−115.
(53) Inoue, C.; Izato, Y.; Miyake, A.; Villermaux, E. Direct Self-Sustained Fragmentation Cascade of Reactive Droplets. *Phys. Rev. Lett.* **2017**, *118*, 074502.

https://doi.org/10.1021/acsomega.2c03081
ACS Omega XXXX, XXX, XXX−XXX

(54) Inoue, C.; Koshi, M.; Himeno, T.; Watanabe, T. Investigation on Liquid Atomization Mechanism in Japanese Sparkler "Senko-Hanabi". *Sci. Technol. Energ. Mater.* **2016**, *77*, 51−58.
(55) Reinhardt, K.; Winkler, H. Cerium Mischmetal, Cerium Alloys, and Cerium Compounds Ley, C.; et al., Eds; *Ullmann's Encyclopedia of Industrial Chemistry*; Wiley-VCH: Weinheim, 2000; Vol. *8*.
(56) Sturman, B. T. On the Emitter of Blue Light in Copper-Containing Pyrotechnic Flames. *Propellants, Explos., Pyrotech.* **2006**, *31*, 70−74.
(57) Jennings-White, C. Blue Strobe Light Pyrotechnic Compositions. *Pyrotechnica* **1992**, *XIV*, 33−45.
(58) Juknelevicius, D.; Dufter, A.; Rusan, M.; Klapötke, T. M.; Ramanavicius, A. Study of Pyrotechnic Blue Strobe Compositions Based on Ammonium Perchlorate and Tetramethylammonium Nitrate. *Eur. J. Inorg. Chem.* **2017**, *2017*, 1113−1119.
(59) Liu, X. Study of Impact of Rare Earth Alloy on Fireworks Stability. In *Progress in Safety, Science and Technology Vol IV Part B*; Wang, Y., Huang, P., Mao, Z., Eds.; Science Press: Beijing, 2004, pp 2853−2855.
(60) Xifeng, Y.; Hongda, C.; Haitao, D.; Gede, H.; Dayong, G.; Lang, C. Study on Rare-Earth Alloy Incendiary Agents and their Applications. In *Theory and practice of energetic materials*; Changgen, F., Ed.; *International Autumn Seminar on Propellants, Explosives and Pyrotechnics*; China Science and Technology Press: Beijing, 2001; Vol. *IV*, pp 466−472.
(61) Gordon, T.; Chen, L. C.; Fine, J. M.; Schlesinger, R. B.; Su, W. Y.; Kimmel, T. A.; Amdur, M. O. Pulmonary Effects of Inhaled Zinc Oxide in Human Subjects, Guinea Pigs, Rats, and Rabbits. *Am. Ind. Hyg. Assoc. J.* **1992**, *53*, 503−509.
(62) Jederlinic, P. J.; Abraham, J. L.; Churg, A.; Himmelstein, J. S.; Epler, G. R.; Gaensler, E. A. Pulmonary Fibrosis in Aluminum Oxide Workers. Investigation of Nine Workers, with Pathologic Examination and Microanalysis in Three of Them. *Am. Rev. Respir. Dis.* **1990**, *142*, 1179−1184.
(63) Hirano, S.; Suzuki, K. T. Exposure, Metabolism, and Toxicity of Rare Earths and Related Compounds. *Environ. Health Perspect.* **1996**, *104*, 85−95.
(64) Hirano, S.; Kodama, N.; Shibata, K.; Suzuki, K. T. Distribution, Localization, and Pulmonary Effects of Yttrium Chloride Following Intratracheal Instillation into the Rat. *Toxicol. Appl. Pharmacol.* **1990**, *104*, 301−311.
(65) Ball, R. A.; Van Gelder, G. Chronic Toxicity of Gadolinium Oxide for Mice Following Exposure by Inhalation. *Arch. Environ. Health* **1966**, *13*, 601−608.
(66) Haque, N.; Hughes, A.; Lim, S.; Vernon, C. Rare Earth Elements: Overview of Mining, Mineralogy, Uses, Sustainability and Environmental Impact. *Resources* **2014**, *3*, 614−635.
(67) Rare earth prices in February 2020. (accessed 02 23, 2022). https://en.institut-seltene-erden.de/rare-earth-prices-in-february-2020.
(68) Prices of Main Light Rare Earth Products and Sintered NdFeB in Baotou in the First Half of July 2021. (accessed 02 23, 2022). https://news.metal.com/newscontent/101544440/Prices-of-main-light-rare-earth-products-and-sintered-NdFeB-in-Baotou-in-the-first-half-of-July-2021.
(69) GoCIE, V2, Thomas, K. R. J., Department of Chemistry, Indian Institute of Technology Roorkee, India, 2009. (accessed 02 23, 2022).https://faculty.iitr.ac.in/~krjt8fcy/gocie.html.

https://doi.org/10.1021/acsomega.2c03081
ACS Omega XXXX, XXX, XXX−XXX